Acta Pharmaceutica Sinica B 2020;10(11):2246–2257

Chinese Pharmaceutical Association
Institute of Materia Medica, Chinese Academy of Medical Sciences

Acta Pharmaceutica Sinica B

www.elsevier.com/locate/apsb
www.sciencedirect.com

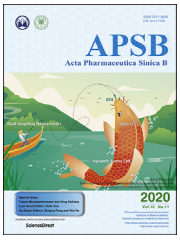

SHORT COMMUNICATION

Phospholipid membrane-decorated deep-penetrated nanocatalase relieve tumor hypoxia to enhance chemo-photodynamic therapy

Junjing Yin[a,b,†], Haiqiang Cao[b,†], Hong Wang[b], Kaoxiang Sun[a,*], Yaping Li[a,b], Zhiwen Zhang[b,c,*]

[a]*School of Pharmacy, Yantai University, Yantai 264005, China*
[b]*State Key Laboratory of Drug Research & Center of Pharmaceutics, Shanghai Institute of Materia Medica, Chinese Academy of Sciences, Shanghai 201203, China*
[c]*Yantai Key Laboratory of Nanomedicine & Advanced Preparations, Yantai Institute of Materia Medica, Yantai 264000, China*

Received 13 March 2020; received in revised form 12 May 2020; accepted 24 May 2020

KEY WORDS

Photodynamic therapy;
Tumor hypoxia;
Catalase;
Tumor penetration;
Drug delivery;
Nanoparticle;
Tumor targeting;
Cancer metastasis;
Cancer therapy

Abstract Hypoxia is a serious impediment to current treatments of many malignant tumors. Catalase, an antioxidant enzyme, is capable of decomposing endogenous hydrogen peroxide (H_2O_2) into oxygen for tumor reoxygenation, but suffered from *in vivo* instability and limited delivery to deep interior hypoxic regions in tumor. Herein, a deep-penetrated nanocatalase-loading $DiIC_{18}$ (5, DiD) and soravtansine (Cat@PDS) were provided by coating catalase nanoparticles with PEGylated phospholipids membrane, stimulating the structure and function of erythrocytes to relieve tumor hypoxia for enhanced chemo-photodynamic therapy. After intravenous administration, Cat@PDS preferentially accumulated at tumor sites, flexibly penetrated into the interior regions of tumor mass and remarkably relieved the hypoxic status in tumor. Notably, the Cat@PDS + laser treatment produced striking inhibition of tumor growth and resulted in a 97.2% suppression of lung metastasis. Thus, the phospholipids membrane-coated nanocatalase system represents an encouraging nanoplatform to relieve tumor hypoxia and synergize the chemo-photodynamic cancer therapy.

*Corresponding authors.
E-mail addresses: sunkaoxiang@luye.com (Kaoxiang Sun), zwzhang0125@simm.ac.cn (Zhiwen Zhang).
†These authors contributed equally to this work.
Peer review under the responsibility of Chinese Pharmaceutical Association and Institute of Materia Medica, Chinese Academy of Medical Sciences.

https://doi.org/10.1016/j.apsb.2020.06.004

1. Introduction

Tumor hypoxia, characterized by reduced oxygen (O_2) levels in tumor, is one of the major hallmarks of malignant solid tumors[1−4]. Hypoxia is usually originated from the fast oxygen consumption by wild proliferation of cancer cells and inadequate oxygen supply from the disordered tumor vasculature[3,5]. Of note, the aberrant metabolism of cancer cells produced large amount of hydrogen peroxide (H_2O_2) in tumor regions with the concentration ranging from ∼50 to 100 μmol/L[6]. Upon hypoxic status, cancer cells would undergo genomic alternations to survive in hypoxic microenvironments, and upregulate versatile transcription factors to promote their malignant progression and metastasis[2,7−10]. Moreover, hypoxia can make cancer cells more resistant to many current therapeutic modalities, such as chemotherapy, radiotherapy and photodynamic therapy (PDT), etc, thereby leading to poor clinical prognosis[4,11−13]. Especially for PDT, the therapeutic effects are achieved by converting oxygen into cytotoxic singlet oxygen ($^1O_2$) upon light irradiation by using versatile photosensitizers (PS), wherein the oxygen in tumor regions presents an essential helper component to fuel the PDT efficacy[14−19]. Unarguably, how to relieve the unfavorable tumor hypoxia and improve the local oxygen levels in tumor is highly desired for effective cancer therapy.

Considering the high concentration of H_2O_2 in tumor regions (∼50−100 μmol/L), *in situ* decomposing H_2O_2 into oxygen can be an intriguing strategy to relieve the tumor hypoxia and increase the oxygen levels in tumor[20−23]. Specially, catalase (CAT) is a heme-containing homotetrameric enzyme that is practically present in mammalian erythrocytes and has high enzyme activities upon their circulation in blood[24,25]. The catalase in erythrocytes is capable of converting dangerous H_2O_2 into water and oxygen to protect them from damage by endogenous H_2O_2[26], thereby holding great potential for tumor oxygenation to enhance the antitumor outcomes. However, the delivery of catalase to tumor sites are suffering from the *in vivo* instability due to the presence of numerous physiological proteases, rapid deactivation of enzyme activities and poor half-life in blood circulation. Although catalase can be encapsulated into porous inorganic nanomaterials, polymeric nanoparticles or albumin nanoparticles for tumor targeted delivery[20,21,27−31], the relative enzymatic activities is often decreased within a few hours and their application still remains a great challenge.

Another obstacle is that the hypoxic regions are heterogeneously distributed in tumor and often located at approximately 100 μm away from a functional blood vessel, the distance beyond the range of oxygen diffusion[32,33]. Although nanoparticles can specifically accumulate at tumor sites, they are usually restricted around the tumor vessels and unable to penetrate into deep interior hypoxic regions[34−37]. Compelling evidence reveals that the poor penetration of nanoparticles in solid tumors is a main cause of their inadequate therapeutic efficacy[34,38,39]. Thereby, the nanoparticles of catalase should be rationally designed to keep the vigorous activity and facilitate their permeation into deep hypoxic regions to decompose endogenous H_2O_2 for tumor oxygenation to enhance the antitumor efficacy.

Inspired by the core-membrane structure of erythrocytes with high catalase activities and their long circulating capability in blood, we herein developed a deep penetrated nanocatalase system by coating catalase nanoparticles with PEGylated phospholipids membrane to relieve tumor hypoxia for enhanced chemo-photodynamic therapy (Scheme 1). The hydrophobic photodynamic agent of DiD and cytotoxic soravtansine were embedded in the phospholipid membrane of 1,2-distearoyl-*sn*-glycero-3-phosphoethanolamine-*N*-[methoxy(polyethylene glycol)-2000] (DSPE-PEG), and then camouflaged onto the surface of catalase nanoparticles to developed the nanocatalase system of DiD and soravtansine (Cat@PDS). The outer phospholipid membrane in Cat@PDS was used to protect catalase from degradation by physiological proteases and ensure their high enzymatic activity. Upon their preferential accumulation at tumor sites, Cat@PDS would penetrate into deep interior hypoxia regions and decompose excessive H_2O_2 into oxygen to relieve the hypoxic status and boost the combinational chemo-photodynamic therapy.

2. Methods

2.1. Materials

Bovine liver catalase (CAT) was purchased from Sigma (New York, USA); DSPE-PEG was supplied by Shanghai Advanced Vehicle Technology Pharmaceutical Ltd. (Shanghai, China). Soravtansine was purchased from Bright Gene Bo Rui Medicine (Suzhou, China). DiD, Annexin V-FITC/PI apoptosis kit and singlet oxygen sensor green (SOSG) were offered by Dalian Meilun Biotechnology Co., Ltd. (Dalian, China).

The murine 4T1 breast cancer cells were supplied by Cell Bank of Shanghai, Chinese Academy of Science (CAS, Shanghai, China). The cancer cells were cultured in RPMI1640 media supplemented with 10% fetal bovine serum (FBS, Gibco, Auckland, New Zealand) and 100 U/mL of penicillin G sodium salt, and 100 μg/mL of streptomycin sulfate (Meilun, Dalian, China) at 37 °C in a humidified incubator containing 5% CO_2.

Female nude mice (18−22 g) were provided by Shanghai Experimental Animal Center, CAS (Shanghai, China). The animals were acclimatized in the animal care facility for 3−5 days prior to the experiments. All the *in vivo* experiment protocols were approved by the Institutional Animal Care and Use Committee (IACUC) of Shanghai Institute of Materia Medical (SIMM), CAS, China.

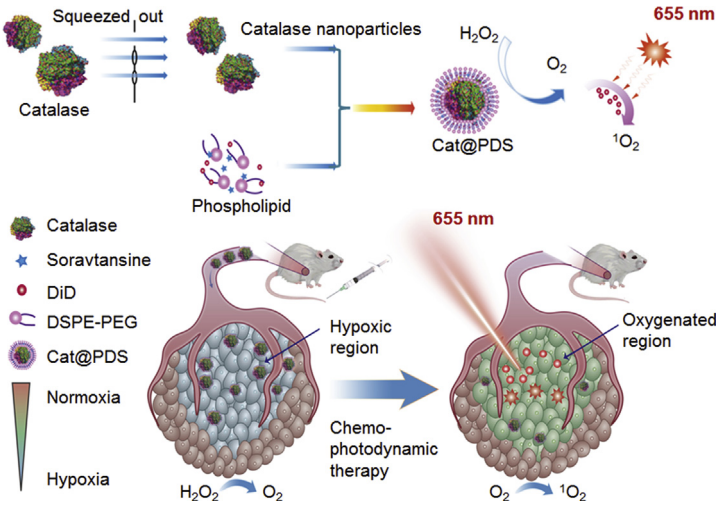

Scheme 1 Schematic illustration of phospholipid membrane coated nanocatalase system (Cat@PDS) to relieve tumor hypoxia for enhanced chemo-photodynamic therapy. Cat@PDS was prepared by coating catalase nanoparticles with phospholipid membrane to keep the high enzymatic activity and facilitate their accumulation at tumor sites. Moreover, Cat@PDS could penetrate into the deep hypoxic regions of tumor mass and decompose endogenous H_2O_2 into oxygen, thereby relieving tumor hypoxic status for enhanced chemo-photodynamic therapy.

2.2. *Preparation and characterization of Cat@PDS*

Cat@PDS is prepared in two steps: (1) dissolving catalase in phosphate buffer saline (PBS, pH 7.4) at 37 °C and squeezing through polycarbonate membrane with the pore size of 400 and 200 nm successively (LiposoFast-Basic, Avestin, Ottawa, Canada) to form the bare catalase nanoparticles; (2) DSPE-PEG, soravtansine and DiD (60: 0.05: 0.2, *w/w*) were dissolved in dichloromethane, and then evaporated into dryness to form a uniform thin film in a round flask. The film was incubated with the bare catalase nanoparticles at 37 °C for 4 h, and then extruded through the polycarbonate membrane (0.2 μm) to obtain the Cat@PDS for further measurements. The terminal concentration of DiD was 200 μg/mL and that of soravtansine was 50 μg/mL.

Because of the interference of DiD on the particle size measurements, only DSPE-PEG was used to fabricate the counterpart Cat@P to optimize the phospholipid/catalase ratio in Cat@PDS formulation. The phospholipid/catalase ratio (*w/w*) was designed at 1.5, 2.25 and 3 to prepare Cat@P and then measured by dynamic light scattering (DLS) analysis on a Nano ZS90 instrument (Malvern, Worcestershire, UK) to record the mean diameter and PDI values. The phospholipid/catalase ratio was optimized as 3 for further measurements.

The morphology of Cat@PDS was determined by transmission electron microscopy (120KV TEM, FEI Talos L120C, Thermo Fisher, Waltham, MA, USA). The absorption profiles of DiD, catalase nanoparticles and Cat@PDS at 0.4 μg/mL DiD or 0.4 mg/mL catalase were monitored using the ultraviolet-visible spectrophotometer (UV-2450 SHIMADZU, Kyoto, Japan) to detect the impact of Cat@PDS on the maximal absorption of photodynamic agent of DiD. Then, the production of singlet oxygen from Cat@PDS, free DiD and PBS was measured using the probe of SOSG to evaluate the photodynamic activity. These samples were mixed with SOSG at 2 μg/mL DiD and 10 μmol/L SOSG, and then exposed to 655 nm laser at 1.0 W/cm^2 for 12 min. At certain time intervals, samples were collected and analyzed on a microplate reader (Ex/Em 504/525 nm, Enspire, Perkin−Elmer, Singapore). All examinations were performed in triplicate.

To determine the encapsulation efficiency (EE) of soravtansine or DiD in Cat@PDS, Cat@PDS was filtered through a 0.22 μm membrane to remove the unentrapped active agents of soravtansine or DiD. The amount of soravtansine in the filtration was determined by a high performance liquid chromatography (HPLC) method on Agilent 1200 system (Agilent, Palo Alto, CA, USA) under the following condition: column, Agilent SD-C18 RRHD (1.8 μm, 100 mm × 2.1 mm); column temperature, 40 °C; mobile phase, methanol-water with 0.1% trifluoroacetic acid (80:20, *v/v*); flow rate, 0.25 mL/min; detection wavelength was 245 nm. Meanwhile, the amount of DiD in the filtration was monitored using a fluorescence analysis on a microplate reader (Enspire, PerkinElmer, Singapore).

Then, the release profiles of soravtansine or DiD from Cat@PDS were measured in the mimicked physiological fluids of PBS (pH 5.5), PBS (pH 7.4) and 100% FBS. In brief, Cat@PDS was diluted with PBS (pH 5.5), PBS (pH 7.4) and 100% FBS for 10 times and then incubated at 37 °C for 12 h. At predetermined time points, samples were collected and the amount of soravtansine or DiD were respectively quantified by HPLC method or fluorescence analysis as aforementioned above.

Importantly, the enzymatic activity of catalase in Cat@PDS is the essential prerequisite for converting H_2O_2 into oxygen for tumor oxygenation. To detect the ability of Cat@PDS on protecting the activity of catalase, bare catalase nanoparticles and Cat@PDS were respectively incubated in PBS (pH 7.4) at 37 °C for 48 h. At predetermined time intervals, samples were collected and the biological activity of catalase were determined using the catalase assay kit according to the manufacturer's protocols (Nanjing jiancheng bioengineering institute, Nanjing, China).

2.3. *Cellular uptake and in vitro therapeutic efficacy of Cat@PDS*

The cellular uptake of free DiD and Cat@PDS was measured in murine 4T1 cancer cells under laser confocal scanning microscope (LCSM, Leica TCS-SP8 STED, Wetzlar, Germany), which depicted as red signals in the captured images. In brief, the 4T1 cells were seeded into a 24-well plate with a sterile round glass coverslip at a density of 2 × 10^5 cells per well and incubated

overnight. Free DiD and Cat@PDS were added to each well at 0.2 μg/mL of DiD and incubated for further 6 h. Then, cells were fixed with 4% paraformaldehyde and stained with 4′,6-diamino-2-phenyl indole (DAPI, Beyotime, Shanghai, China) for observation under LCSM. Meanwhile, the uptake of free DiD and Cat@PDS in 4T1 cancer cells were quantified by flow cytometry (BD LSR Fortessa 18-color laser, San Jose, CA, USA). Cells without any treatments were used as negative control. All the experiments were performed in triplicate.

Then, to evaluate the photodynamic activity of Cat@PDS in 4T1 cancer cells, cells were seeded to 24-well plate with a round coverslip in each well at a density of 2×10^5 cells/well and incubated overnight. Free DiD and Cat@PDS were added to each well at 0.2 μg/mL of DiD and incubated at 37 °C for 4 h. Then, cells were replaced with fresh culture media and incubated with the singlet oxygen probe of 2,7-dichlorodi-hydrofluorescein diacetate (DCFH-DA, Thermo Fisher, Wilmington, DE, USA) for 30 min. Afterwards, cells were exposed to 655 nm laser at 1.0 W/cm^2 for 2 min. Cells were counterstained with DAPI for visualization under LCSM to detect the production of reactive oxygen species (ROS, green fluorescence signals). Meanwhile, the production of ROS in 4T1 cells was quantified by flow cytometer analysis (BD LSR Fortessa 18-color laser, San Jose, CA, USA).

The impact of Cat@PDS mediated chemo-photodynamic therapy on cell apoptosis were determined in 4T1 cancer cells by flow cytometry (FACSCalibur system, BD). Cells were seeded into a 24-well plate at 2×10^5 cells per well and cultured overnight. To examine the impact of laser irradiation power density, Cat@PDS was added to each well at 25 ng/mL soravtansine and 100 ng/mL of DiD and incubated for 4 h. Then, the pretreated cells were irradiated with 655 nm with a power of 0.4, 0.7 and 1.0 W/cm^2 for 2 min, and then stained with the cell apoptosis assay kit. The percentage of cell apoptosis at early and late stages of apoptosis were monitored by flow cytometry (FACSCalibur system, BD). The PBS-treated cells without laser irradiation were performed as negative control. Then, to verify the synergistic effects of Cat@PDS-mediated combination therapy, Cat@PDS, Cat@PD and Cat@P were added to each well at 40 ng/mL of DiD and 100 ng/mL of DiD, or comparable to 10 and 25 ng/mL soravtansine, respectively, and then incubated for 4 h. Afterward, the pretreated cells were exposed to 655 nm laser at a power density of 0.7 W/cm^2 for 1 min. Two hours later, samples were collected and the percentage of apoptotic cells was quantified by the flow cytometer analysis.

2.4. *In vivo tumor accumulation and intratumoral permeation of Cat@PDS*

The specific tumor accumulation and intratumoral permeation of Cat@PDS were measured in 4T1-induced tumor bearing mice, which was developed by subcutaneous injection of 4T1 cells to the secondary mammary glands at 1×10^6 cells per mouse. When the tumor volume reached 100 mm^3, mice were respectively injected with free DiD or Cat@PDS at 1.0 mg/kg of DiD *via* tail vein. At predetermined time points, mice were anaesthetized with isoflurane-O_2 and the red fluorescence signals were recorded using the *in vivo* imaging system (IVIS Spectrum, PerkinElmer, Waltham, MA, USA). Then, at 2, 12 and 24 h of injection, mice were autopsied and the major organs including heart, liver, spleen, lung, kidney and tumor tissues from each treatment were collected and imaged under the *in vivo* imaging system. Meanwhile, the fluorescence intensity from each organ were analyzed for quantification ($n = 3$). At 12 h of injection of free DiD or Cat@PDS at 4.0 mg/kg of DiD *via* tail vein, mice were autopsied and the major organs were collected. Thereafter, these tissues were respectively accurately weighed, homogenized with dimethyl sulfoxide (1:3, *w/w*) and centrifuged at 3000×*g* for 5 min (Thermo Fisher Scientific, Osterode, Germany) to collect the supernatant. The fluorescence intensity of DiD from these supernatant was quantified using the microplate reader (Enspire, Perkin−Elmer, Singapore).

Then, the intratumoral permeation of Cat@PDS were determined using LCSM detection. The tumor tissues were collected at 12 h after injection of free DiD or Cat@PDS (1.0 mg/kg of DiD), embedded in tissue optimal cutting temperature (OCT) compound for cryostat section at 10 μm (Leica CM1950, Wetzlar, Germany). The sections were fixed with 4% paraformaldehyde for 15 min and counterstained with DAPI for visualization under LCSM. The fluorescence signals of the whole tumor sections, at interior regions and outer edges of tumor mass were collected to record the distribution profiles of Cat@PDS in tumor, wherein Cat@PDS was shown as red fluorescence signals and the nuclei were denoted as blue signals. Thereafter, the intratumoral distribution of red fluorescence signals from free DiD and Cat@PDS were analyzed using the Image J software (National Institutes of Health, Bethesda, MD, USA).

2.5. *In vivo efficacy of Cat@PDS on relieving tumor hypoxia*

The efficacy of Cat@PDS on relieving hypoxic status in tumor were measured in 4T1-induced tumor model as described above. At first, the oxygen level in tumor was monitored using photoacoustic imaging analysis (Vevo LAZR, VisualSonic FUJIFILM, Toronto, Canada). At 4 and 12 h after injection of Cat@PDS at 1.0 mg/kg of DiD *via* tail vein, mice were anaesthetized and the signals of oxyhemoglobin were recorded to characterize the oxygen levels in tumor (blue signals). Meanwhile, at 12 h after injection of PBS control or Cat@PDS, the tumor tissues were collected and the catalase activity in tumor were determined using the catalase assay kit according to the manufacturer's protocols (Nanjing jiancheng bioengineering institute, Nanjing, China).

To detect the impact of Cat@PDS treatment on HIF-1α expression, a surrogate marker of tumor hypoxia, the tumor bearing mice were intravenously administered with free DiD and Cat@PDS at 1.0 mg/kg of DiD at Days 1, 3 and 5, following with laser irradiation (1.0 W/cm^2) at 12 h after the injection. Then, the tumor tissues from each treatment were collected, embedded in paraffin and sectioned (RM2235, Leica, Wetzlar, Germany) for further detections. The sections were respectively incubated with primary antibody of anti-HIF-1α (GTX127309, GeneTex, 1:500, Alton Pkwy Irvine, CA, USA) and secondary antibody of Alexa Fluor 488-labeled goat-anti-rabbit IgG (H + L, Jackson, 111-545-003, 1:400, West Grove, PA, USA). Afterward, the sections were counterstained with DAPI for visualization under fluorescence microscope (Leica DM68, Wetzlar, Germany). The expression of HIF-1α was denoted as green signals in the captured images.

Encouraged by the increased oxygen level and reduced HIF-1α expression in tumor, the production of singlet oxygen in Cat@PDS treated tumor was detected using the ROS probe of DCFH-DA (Thermo Fisher scientific). Twelve hours after injection of free DiD or Cat@PDS, 25 μL of DCFH-DA (10 μmol/L) was intratumorally injected to the tumor sites. Thirty minutes later, the tumor tissues from free DiD and Cat@PDS treated group were exposed to 655 nm laser at 1.0 W/cm^2 for 5 min. Then, the

tumor tissues were collected, embedded in OCT and sectioned at 10 μm (Leica 1950, Wetzlar, Germany). These sections were fixed with 4% paraformaldehyde and counterstained with DAPI for LCSM detections, wherein the production of singlet oxygen was presented as green signals.

2.6. *In vivo therapeutic effect of Cat@PDS-mediated chemo-photodynamic therapy on tumor growth and lung metastasis*

The therapeutic effects of Cat@PDS-mediated chemo-photodynamic therapy on tumor growth and lung metastasis was measured in 4T1-induced tumor model as described above. When the tumor volume reached 100 mm^3, mice were respectively treated with PBS control, Cat@P, Cat@PD + laser, Cat@PDS and Cat@PDS + laser by intravenous injection (DiD:1.0 mg/kg, DM4: 0.25 mg/kg, $n = 5$). In laser-treated group, the tumor tissues were exposed to 655 nm laser irradiation at 1.0 W/cm^2 for 5 min at 12 h after injection. The treatments were implemented every 3 days (Days 1, 3 and 6) up to three times in total. The tumor volume was monitored using a digital caliper and the body weights were documented. When the tumor volume in PBS group was over 1500 mm^3 at day 18 after the first treatment, the experiments were discontinued. The tumor growth index was calculated by comparing the tumor volume at the end point to that at the beginning time of treatments. At the end, mice were autopsied and the tumor tissues from each treatment were collected and weighed to calculate the inhibitory rate on tumor growth. Moreover, the lungs from each treatment were collected and photographed. The number of visualized metastatic nodules in lungs from each treatment was recorded to evaluate the therapeutic effects on suppressing lung metastasis. Histological examinations of the lungs from each group were implemented to detect the incidence of metastatic lesions. In addition, histological examinations of other major organs of heart, liver, spleen and kidney were also performed by H&E staining method to evaluate the biosafety of each treatment.

2.7. *Statistical analysis*

Data were presented as mean ± standard deviation (SD). Student's two-tailed *t*-test was used to analyze the difference between two groups while analysis of variance (ANOVA) was utilized for multiple comparisons. Statistical difference was considered as $P < 0.05$ and very significance as $P < 0.01$.

3. Results and discussion

3.1. *Preparation and characterization of Cat@PDS*

Initially, Cat@PDS was fabricated in two steps: (1) squeezing the catalase suspension in PBS (pH 7.4) through polycarbonate membrane with the pore size of 400 and 200 nm successively to obtain the bare catalase nanoparticles; (2) coating catalase nanoparticles with the lipid membrane of DSPE-PEG, DiD and soravtansine to develop the Cat@PDS. The particle size distribution of nanoparticles was measured by DLS analysis. Although bare catalase nanoparticles were nano-sized particles with a mean diameter of 97.14 ± 30.49 nm, they tended to aggregate into larger particles with a wide size distribution after their storage in PBS (pH 7.4, Supporting Information Fig. S1). Due to the interference of DiD on DLS analysis, the blank formulation of Cat@P was used for optimizing the phospholipids/catalase ratio in the formulation. By measuring the mean diameter, polydispersivity index (PDI) and their variations with time, the phospholipids/catalase ratio in Cat@P was optimized at 3:1 (*w/w*, Supporting InformationFigs. S2−S3). At the optimized phospholipid/catalase ratio, Cat@P displayed a hydrodynamic Z-average size of 162.4 nm with a PDI value of 0.21. When they were incubated in PBS at pH 7.4 for 24 h, the mean diameter and the PDI values were barely changed, suggesting their good stability in the mimicked physiological fluids (Fig. 1A). Meanwhile, the morphology of Cat@PDS was visualized under transmission electron microscope (TEM), which showed Cat@PDS was nanometer-sized particles (Fig. 1B). The good stability of Cat@PDS in PBS (pH 7.4) could be largely ascribed to the core−membrane structure and the coated phospholipid membrane in Cat@PDS.

Both DiD and soravtansine were loaded in the outer phospholipid membrane of Cat@PDS due to the hydrophobic interactions, which was determined by HPLC and fluorescence analysis. The measured results indicated that the cytotoxic soravtansine was loaded in Cat@PDS with an encapsulation efficiency (EE) value of 98.15 ± 1.15% and drug loading (DL) capacity of 0.061 ± 0.001%, while the photodynamic agent of DiD was loaded in Cat@PDS with a EE value of 97.45 ± 0.90% and DL value of 0.243 ± 0.002%, respectively, suggesting their high entrapments in the Cat@PDS system. When they were incubated in mimicked physiological fluids of PBS (pH 5.5), PBS (pH 7.4) and 100% FBS, the cumulative release of soravtansine was less 15% in these mimicked physiological fluids at 12 h of incubation (Fig. 1C). Concurrently, the cumulative release of DiD was less than 20% in PBS at pH 5.5 and 7.4, but slightly increased to 21.7% in FBS (Fig. 1D). These experimental data suggested that about 80% of therapeutic DiD or soravtansine could remain inside the Cat@PDS system upon their incubation in the mimicked physiological fluids, which would be favorable for *in vivo* delivery and specific tumor accumulation.

In the absorption profiles, both free DiD and Cat@PDS showed maximum absorption at 655 nm, but the bare catalase nanoparticles showed negligible absorption at this wavelength (Fig. 1E). The high absorption of Cat@PDS at 655 nm could be beneficial for producing cytotoxic $^1O_2$ upon 655 nm laser irradiation to exert the photodynamic therapy. Accordingly, we examined the photodynamic activity of Cat@PDS and free DiD upon their exposure to 655 nm laser using a ROS probe of SOSG (Supporting Information Fig. S4). The $^1O_2$ production in Cat@PDS was generally increased with the irradiation time and more efficient *versus* free DiD, which would be conducive to exerting the pharmacological activities.

Of note, the catalase activity in Cat@PDS is an essential prerequisite for decomposing endogenous H_2O_2 and relieving tumor hypoxia. The catalase activity of catalase nanoparticles and Cat@PDS were measured using a catalase assay kit. The bare catalase nanoparticles and Cat@PDS were respectively incubated in PBS (pH 7.4) at 37 °C and the catalase activity were monitored at certain time intervals. Upon their incubation in PBS (pH 7.4) for 48 h, the relative catalase activity in Cat@PDS was barely changed, but that in catalase nanoparticles was dramatically reduced to only 51.2 ± 5.0% (Fig. 1F). These data suggested the catalase in Cat@PDS showed a high enzymatic activity, which could be mainly ascribed to the coating of phospholipid membrane in Cat@PDS. The high catalase activity in Cat@PDS would be favorable to decompose excessive endogenous H_2O_2 for tumor reoxygenation.

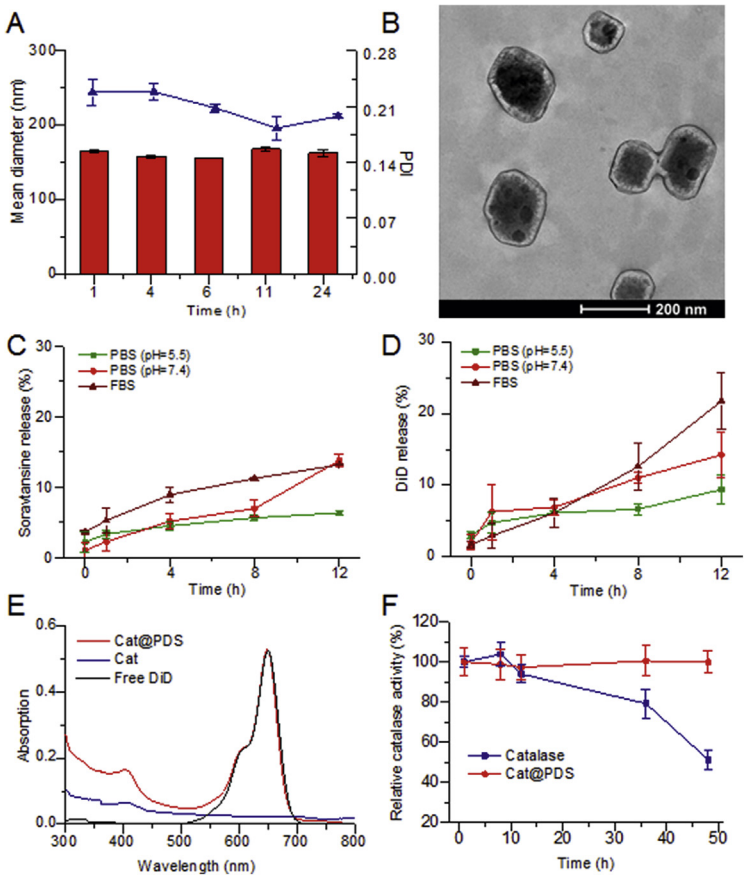

Figure 1 Characterization of Cat@PDS. (A) Variation of mean diameter and PDI values of Cat@P upon their incubation in PBS (pH 7.4) for 24 h. Data are mean ± SD (n = 3); (B) Typical TEM images of Cat@PDS, scale bar = 200 nm; (C) Cumulative release profiles of soravtansine from Cat@PDS in mimicked physiological fluids of PBS (pH 5.5), PBS (pH 7.4) and FBS. Data are mean ± SD (n = 3); (D) Cumulative release profiles of DiD from Cat@PDS in PBS (pH 5.5), PBS (pH 7.4) and FBS. Data are mean ± SD (n = 3); (E) The absorption profiles of Cat@PDS, catalase and free DiD within the wavelength of 300−800 nm; (F) Relative catalase activity of catalase nanoparticles and Cat@PDS upon their incubation in PBS (pH 7.4) for 48 h. Data are mean ± SD (n = 3).

3.2. *In vitro evaluation of Cat@PDS in 4T1 cancer cells*

The cellular uptake of Cat@PDS and free DiD was measured in 4T1 breast cancer cells by LCSM and further quantified by flow cytometer analysis (Fig. 2). In the captured images, the red signals of DiD from Cat@PDS were extensively detected inside the 4T1 cancer cells with the fluorescence intensity much stronger than that from free DiD group (Fig. 2A). The flow cytometry analysis results showed the mean fluorescence intensity from Cat@PDS was remarkably enhanced by 8.8-fold and 5.2-fold *versus* free DiD treatment at 4 and 12 h of incubation, respectively (Fig. 2B). The higher uptake of Cat@PDS over free DiD could be resulted from the efficient incorporation of DiD into the nanometer-sized particle system of Cat@PDS.

Then, the production of ROS was determined using the DCFH-DA probe, which would present as green fluorescence signals under LCSM upon their interactions with ROS. When the Cat@PDS pretreated cells were exposed to 655 nm laser at 1.0 W/cm^2 for 2 min, a large amount of green signals was readily detected with the intensity higher than free DiD treatment (Fig. 2C). Meanwhile, the flow cytometer analysis showed the mean fluorescence intensity from Cat@PDS treated cells were enhanced by 4.3- and 6.3-fold *versus* that from free DiD group at 4 and 12 h of incubation, respectively (Fig. 2D). The efficient ROS production from Cat@PDS-treated group over free DiD could be mainly ascribed to the improved uptake in 4T1 cancer cells.

Afterwards, the therapeutic effects of Cat@PDS-mediated combination therapy were evaluated by apoptosis of 4T1 cancer cells using flow cytometry analysis (Fig. 2E). To detect the impact of laser irradiation power density, the Cat@PDS-treated cells were exposed to 655 nm laser at 0.4, 0.7 and 1.0 W/cm^2 and the percentage of apoptotic cells were monitored by flow cytometry (Supporting Information Fig. S5). Cell apoptosis was considerably detected in these samples and the apoptosis percentage was increasing with the power of laser irradiation, which could reach at 58.53% at 0.7 W/cm^2. Then, to verify the superiority of Cat@PDS mediated combination therapy, cells were respectively treated with Cat@PDS, Cat@PD and Cat@P at 40 ng/mL of DiD (comparable to 10 ng/mL soravtansine) and 100 ng/mL of DiD (comparable to 25 ng/mL soravtansine) at 0.7 W/cm^2, respectively. The percentage of apoptotic cells in Cat@PDS mediated combination therapy (Cat@PDS + laser) was 6.19- and 9.60-fold higher than counterpart Cat@PD + laser group and un-irradiated Cat@PDS group at 40 ng/mL of DiD (comparable to 10 ng/mL soravtansine), which effectively confirmed the superiority of Cat@PDS + laser over other counterpart formulations (Fig. 2E). The superior effectiveness of Cat@PDS mediated combination therapy was also validated at 100 ng/mL of DiD (comparable to

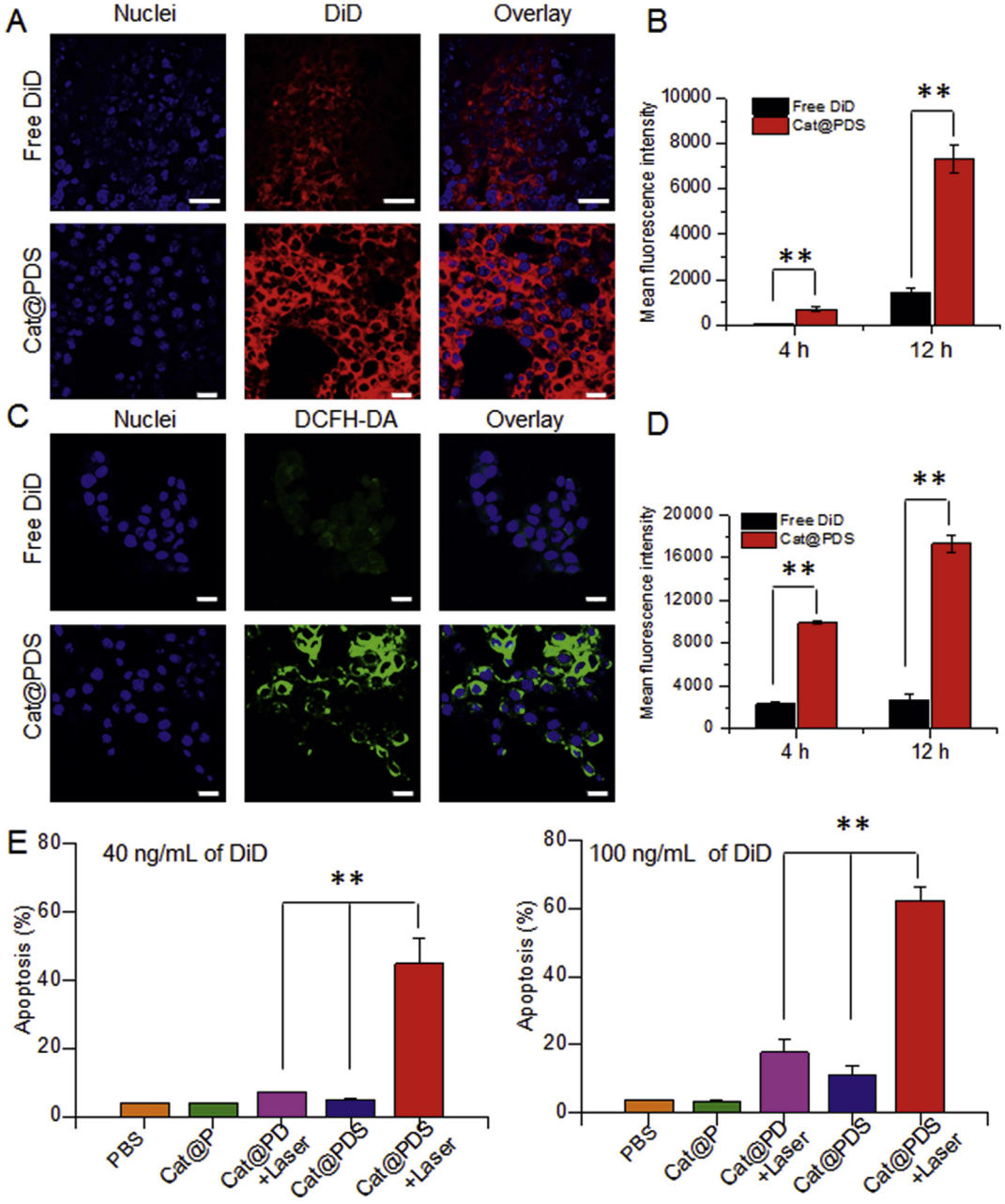

Figure 2 The *in vitro* evaluation of Cat@PDS in 4T1 cancer cells. (A) Cellular uptake of free DiD and Cat@PDS in 4T1 cells by LCSM measurements, scale bar = 20 μm; (B) Quantified cellular uptake of free DiD and Cat@PDS in 4T1 cells by flow cytometer analysis. Data are mean ± SD ($n = 3$), $^{**}P < 0.01$; (C) Production of singlet oxygen in free DiD and Cat@PDS treated 4T1 cells upon their exposure to 655 nm laser, which was denoted as green signals under LCSM, scale bar = 20 μm; (D) The quantified production of singlet oxygen in free DiD and Cat@PDS treated 4T1 cells by flow cytometer analysis. Data are mean ± SD ($n = 3$), $^{**}P < 0.01$; (E) The percentage of cell apoptosis in Cat@PDS mediated combination therapy at 40 ng/mL and 100 ng/mL of DiD. Data are mean ± SD ($n = 3$), $^{**}P < 0.01$.

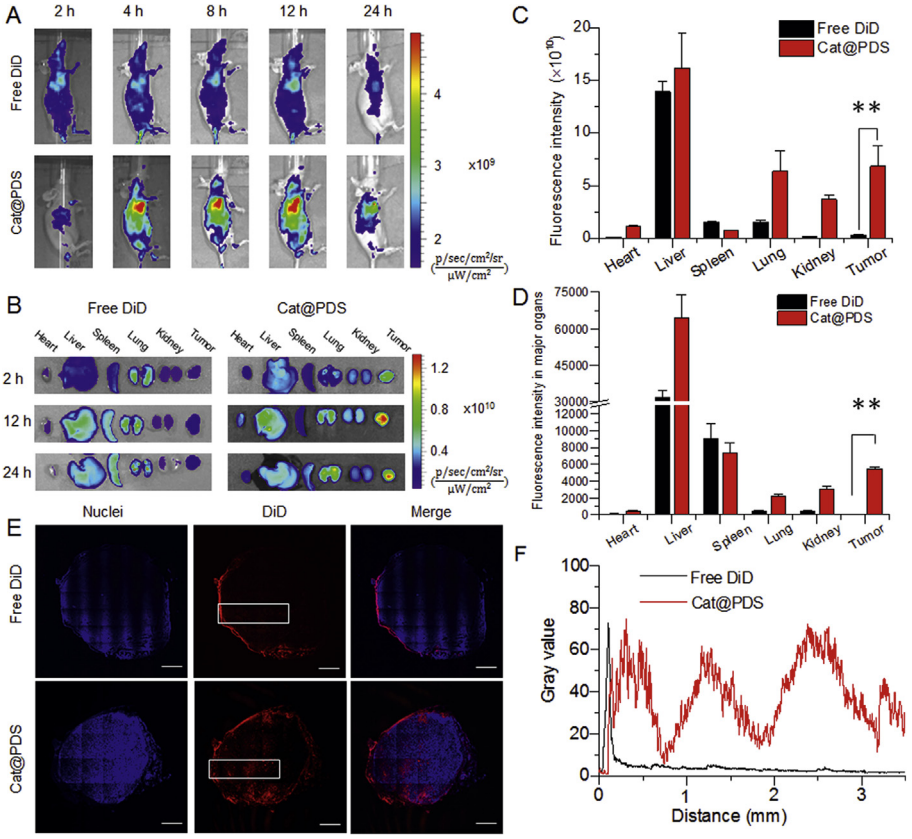

Figure 3 The *in vivo* tumor targeting and intratumoral permeation of Cat@PDS in 4T1-induced tumor bearing mice. (A) The *in vivo* imaging of Cat@PDS in 4T1 tumor model; (B) The *ex vivo* imaging of Cat@PDS in major organs at different time points after injection; (C) The semi-quantitative analysis of free DiD and Cat@PDS in the major organs at 12 h after injection. Data are mean ± SD ($n = 3$), $^{**}P < 0.01$; (D) The quantified distribution of DiD in the major organs from free DiD and Cat@PDS treated groups at 12 h after injection. Data are mean ± SD ($n = 3$), $^{**}P < 0.01$; (E) The intratumoral permeation of Cat@PDS in the tumor mass under LCSM, which was denoted as red signals in the captured images, scale bar = 1 mm; (F) Image analysis of intratumoral permeation of Cat@PDS in the white rectangle by Image J software.

25 ng/mL soravtansine, Fig. 2E). These data confirmed the efficient cellular uptake of Cat@PDS in 4T1 cancer cells and robust ROS production upon laser irradiation, thereby resulting in noticeable therapeutic effects.

3.3. *Specific tumor accumulation and intratumoral permeation of Cat@PDS*

Next, the specific tumor accumulation and their intratumoral penetration of Cat@PDS were determined in 4T1-induced tumor bearing mice, which was developed by injecting 4T1 cancer cells to the secondary mammary pads at 1×10^6 cells per mouse. The preferential tumor accumulation and their deep permeation into hypoxic regions of tumor mass are the essential prerequisites for relieving hypoxic status in tumor[40–42]. The *in vivo* imaging results showed that the red signals of DiD from Cat@PDS could be readily detected at the tumor sites at 4 h after injection and remain at a high level thereafter (Fig. 3A). At 2, 12 and 24 h after injection, mice were autopsied and the major organs were collected for imaging using the *in vivo* imaging system. The captured images showed that the fluorescence signals of Cat@PDS was highly detected at tumor sites, and the intensity was evidently stronger than that from free DiD group (Fig. 3B). Particularly in tumor sites, the semi-quantitative analysis showed that the fluorescence intensity from Cat@PDS was tremendously improved by 23.65-, 25.62- and 17.5-fold over that of free DiD group at 2, 12 and 24 h of injection, respectively (Fig. 3C and Supporting Information Fig. S6). Moreover, the quantified results indicated that the distribution of Cat@PDS in tumor was remarkably improved 54.1-fold over free DiD (Fig. 3D). The different value between them could be resulted from the variance of detection techniques and data presentations. Encouraged by the high tumor accumulation of Cat@PDS, we further evaluated their intratumoral permeation capacity using LCSM. In the transverse profiles of the whole tumor mass, the red fluorescence signals of Cat@PDS were heterogeneously but ubiquitously distributed in tumor mass with high intensity, wherever in the exterior regions or deep interior areas (Fig. 3E), which was further confirmed by imaging analysis (Fig. 3F). Concurrently, the deeper penetration of Cat@PDS over free DiD was further confirmed with strong red fluoresce signals in exterior and interior regions of tumor mass (Fig. 4). We have recently confirmed the limited intratumoral penetration of liposomal formulation in 4T1 induced tumor model[35,36]. The considerable tumor accumulation and intratumoral permeation of Cat@PDS could be resulted from the endogenous properties of catalase, the nanometric size and the erythrocyte-inspired core-membrane structure. The efficient and specific accumulation of Cat@PDS at tumor sites as well as their flexible permeation in tumor tissues would provide an opportunity to relieve the hypoxic status in tumor and exert the therapeutic effects for cancer therapy.

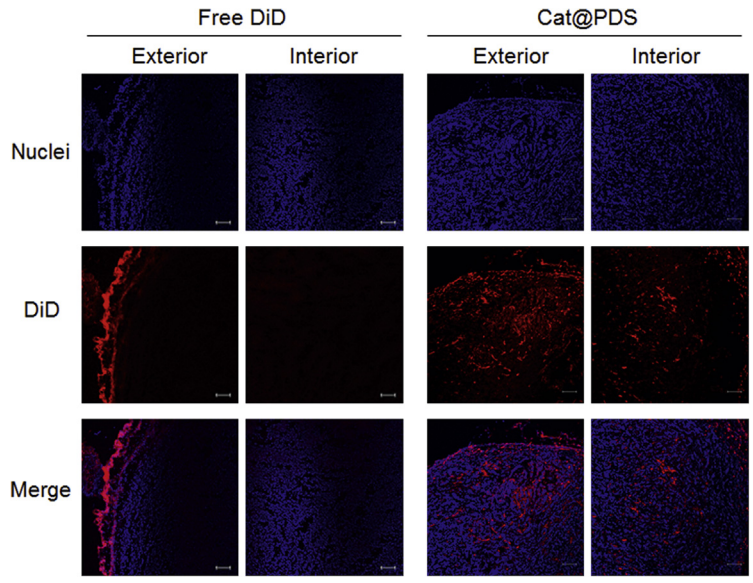

Figure 4 The intratumoral permeation of free DiD and Cat@PDS at exterior and interior regions of tumor mass at 12 h after injection under LCSM, wherein DiD was denoted as red fluorescence signals in the captured images, scale bar = 100 μm.

3.4. *In vivo efficacy of Cat@PDS on relieving tumor hypoxia*

Most importantly, relieving tumor hypoxic status is strikingly needed to ameliorate the therapeutic effects[1,41]. We assessed the ability of Cat@PDS on increasing tumor oxygen level and relieving tumor hypoxia in 4T1 induced tumor model (Fig. 5). The oxygen level in tumor tissues were monitored by photoacoustic imaging, which would present as blue signals in the captured images. As shown in Fig. 5A, the blue signals of oxygen could be detected 4 h after injection of Cat@PDS and reach at a high level at 12 h of injection, suggesting the superior efficiency of Cat@PDS in increasing tumor oxygenation and their ability to

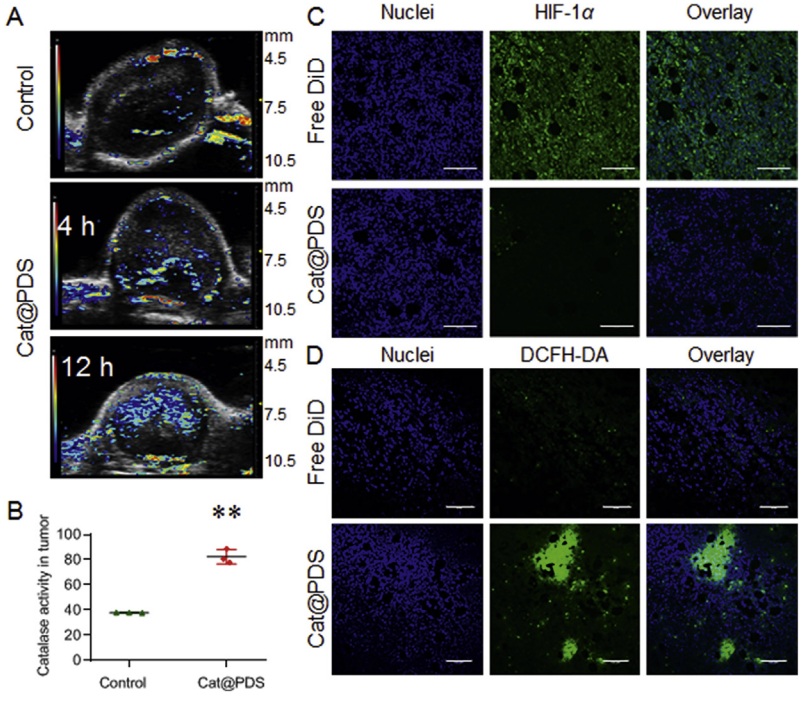

Figure 5 The efficacy of Cat@PDS on relieving hypoxic status in tumor. (A) The increased oxygen level in tumor by Cat@PDS treatment, which was determined by photoacoustic imaging at 4 h and 12 h after injection and denoted as blue signals in the captured images; (B) The catalase activity in tumor from Cat@PDS treated group. Data are mean ± SD ($n = 3$), $^{**}P < 0.01$; (C) The HIF-1α expression in tumor from Cat@PDS treated group, which was denoted as green signals in the captured images, scale bar = 100 μm. (D) Production of singlet oxygen in tumor from Cat@PDS treated group, which was denoted as green signals under LCSM. The tumor tissues were exposed to 655 nm laser at 1.0 W/cm^2 for 5 min for the measurements, scale bar = 100 μm.

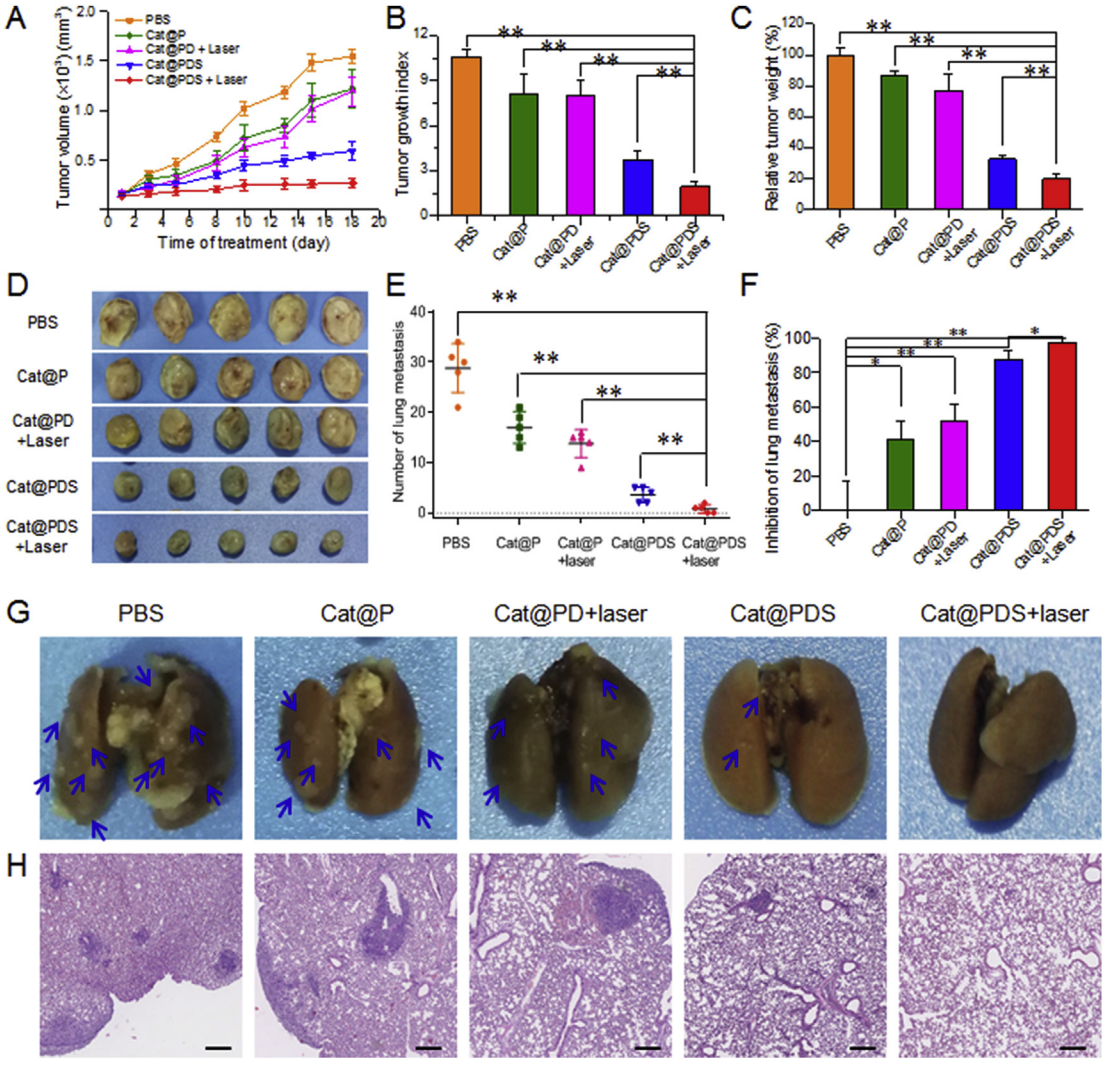

Figure 6 The *in vivo* therapeutic effects of Cat@PDS on tumor growth and lung metastasis of breast cancer in 4T1 induced tumor model. (A) Tumor growth profiles from each treatment. Data are mean ± SD ($n = 5$); (B) The tumor growth index of each treatment at the end time point. Data are mean ± SD ($n = 5$), $^{**}P < 0.01$; (C) The relative tumor weight from each treatment, which was used to characterize the tumor inhibitory effects. Data are mean ± SD ($n = 5$), $^{**}P < 0.01$; (D) The typical photograph of tumor tissues from each treatment; (E) The number of visualized metastatic nodules in lung from each treatment. Data are mean ± SD ($n = 5$), $^{**}P < 0.01$; (F) The inhibitory rate of each treatment on suppressing lung metastasis of breast cancer, which was compared to the PBS control. Data are mean ± SD ($n = 5$), $^{*}P < 0.05$, $^{**}P < 0.01$; (G) Typical photograph of lung tissues from each treatment at the end time point, which was denoted as blue arrows; (H) The H&E examinations of lung tissues from each treatment, wherein the metastatic lesion was presented as cell clusters with darkly stained nuclei, scale bar = 200 μm.

relieve tumor hypoxia. Meanwhile, the catalase activity in tumor from Cat@PDS treated group was evidently improved by 2.17-fold *versus* the control group (Fig. 5B). The increase of oxygen levels in tumor could be mainly attributed to the efficient tumor accumulation, flexible intratumoral permeation and vigorous catalase activity of Cat@PDS. Then, the expression of hypoxia induced factor (HIF)-1α, a surrogate marker of tumor hypoxia[43,44], was measured by immunofluorescence assay to evaluate the performance of Cat@PDS on relieving tumor hypoxic status. As shown in Fig. 5C, the expression of HIF-1α (green signals in the captured images) could be extensively detected with strong intensity in free DiD treated group, but rarely detected in Cat@PDS treated group, suggesting the effectiveness of Cat@PDS in reducing the hypoxic status in tumor. Considering the increased oxygen levels and reduced hypoxic status in tumor by Cat@PDS treatment, we then measured the production of cytotoxic $^1O_2$ upon 655 nm laser irradiation, which was detected using the characteristic probe of DCFH-DA (Fig. 5D). The green signals of $^1O_2$ could be obviously detected in Cat@PDS treated group with high intensity but poorly observed in free DiD group. These data suggested that the Cat@PDS treatment could distinctly enhance the oxygen levels and reduce the hypoxic status, leading to dramatic production of cytotoxic $^1O_2$ for antitumor therapy.

3.5. *In vivo therapeutic efficacy of Cat@PDS on tumor growth and lung metastasis*

Finally, the efficacy of Cat@PDS mediated chemo-photodynamic therapy on tumor growth and metastasis were investigated in 4T1

induced metastatic breast cancer model. The tumor bearing mice were respectively treated with PBS control, Cat@P, Cat@PD + laser, Cat@PDS and Cat@PDS + laser at 1.0 mg/kg of DiD and/or 0.25 mg/kg of soravtansine. For laser irradiated group, the tumor tissues were exposed to 655 nm laser at 1.0 W/cm^2 for 5 min at 12 h of injection. The body weights of tumor bearing mice from each group were not significantly changed during each treatment (Supporting Information Fig. S7). The tumor growth index (TGI) that defined as the ratio of tumor volume at end time point comparing to that at the beginning time point of drug administration was used to characterize the inhibitory effects on tumor growth. As shown in the tumor growth profiles, the Cat@PDS + laser treatment showed remarkable suppression of tumor growth with a TGI value of only 1.9 ± 0.4, which was considerably lower than that of other groups (Fig. 6A and B). Compared to the negative control, the Cat@PDS + laser treatment produced an 82.9% inhibition of tumor growth. Notably, the tumor volume in Cat@PDS + laser treated group was only 44.8% of Cat@PDS group and 22.2% of Cat@PD + laser group, suggesting the superior synergistic effect of Cat@PDS + laser over the counterpart treatments of Cat@PDS and Cat@PD + laser. The synergistic combination efficacy in Cat@PDS + laser *versus* the Cat@PDS and Cat@PD + laser was also confirmed by measuring tumor weight from each treatment (Fig. 6C and D).

Lung is one of the most frequent organs of breast cancer metastasis[45,46]. The effect of Cat@PDS + laser on suppressing the incidence of lung metastasis was also determined. At the end time point, the number of visualized metastatic lesions in each lung was counted to assess the anti-metastasis efficacy. As shown in Fig. 6E and G, the lung metastatic lesions were rarely visualized in Cat@PDS + laser group but obviously detected in other groups. The average number of lung metastasis was only 0.80 ± 0.84 in Cat@PDS + laser group, which was tremendously lower than that of other groups (Fig. 6E). Compared to the PBS control, the Cat@PDS + laser treatment resulted in a 97.2% inhibition of lung metastasis, which was much higher than that of other treatments (Fig. 6F). Moreover, the average number of lung metastasis in Cat@PDS + laser group was only 22.2% of Cat@PDS and 5.8% of Cat@PD + laser treatment, validating the superiority of the synergistic Cat@PDS + laser treatment *versus* the counterpart Cat@PDS and Cat@PD + laser therapy. The incidence of lung metastasis was also measured by hematoxylin and eosin (H&E) assay of the lung from each treatment (Fig. 6H). The metastatic lesions were barely detected in Cat@PDS + laser group but obviously observed in lungs from other treatments. The biosafety of each treatment was confirmed by H&E examinations of the major organs of heart, liver, kidney and spleen after multiple dosing (Supporting Information Fig. S8). Collectively, these data indicated that the Cat@PDS + laser treatment produced efficient inhibitory effects on tumor growth and metastasis, confirming the superior effectiveness of Cat@PDS mediated combinational chemo-photodynamic therapy.

4. Conclusions

In summary, we successively developed a phospholipid membrane-coated nanocatalase system of Cat@PDS with noticeable tumor accumulation and deep intratumoral permeation capability. The Cat@PDS treatment considerably increased the oxygen levels in tumor, reduced the expression of HIF-1α and produced profuse ROS upon laser irradiation. In 4T1-induced tumor model, the Cat@PDS + laser combination treatment resulted in remarkable inhibition of tumor growth and produced a 97.2% suppression of lung metastasis. Thus, the phospholipids membrane-coated nanocatalase system represents a generalizable and convenient nanoplatform to relieve tumor hypoxia and synergize the combinational chemo-photodynamic therapy.

Acknowledgments

This work was financially supported by the Strategic Priority Research Program of CAS (XDA12050307, China), National Natural Science Foundation of China (31771092, 81803444), Youth Innovation Promotion Association of CAS and Fudan-SIMM Joint Research Fund (FU-SIMM20182005, China).

Author contributions

Junjing Yin, Haiqiang Cao and Zhiwen Zhang designed the research. Junjing Yin and Haiqiang Cao carried out the experiments and performed data analysis. Hong Wang participated part of the experiments. Junjing Yin wrote the manuscript. Zhiwen Zhang revised the manuscript. Kaoxiang Sun and Yaping Li supervised the project and interpreted the data. All of the authors have read and approved the final manuscript.

Conflicts of interest

The authors have no conflicts of interest to declare.

Appendix A. Supporting information

Supporting data to this article can be found online at https://doi.org/10.1016/j.apsb.2020.06.004.

References

1. Wang H, Li J, Wang Y, Gong X, Xu X, Wang J, et al. Nanoparticles-mediated reoxygenation strategy relieves tumor hypoxia for enhanced cancer therapy. *J Control Release* 2019;**319**:25–45.
2. Wilson WR, Hay MP. Targeting hypoxia in cancer therapy. *Nat Rev Canc* 2011;**11**:393–410.
3. Nakazawa MS, Keith B, Simon MC. Oxygen availability and metabolic adaptations. *Nat Rev Canc* 2016;**16**:663–73.
4. Liu Y, Jiang Y, Zhang M, Tang Z, He M, Bu W. Modulating hypoxia *via* nanomaterials chemistry for efficient treatment of solid tumors. *Acc Chem Res* 2018;**51**:2502–11.
5. Rey S, Schito L, Koritzinsky M, Wouters BG. Molecular targeting of hypoxia in radiotherapy. *Adv Drug Deliv Rev* 2017;**109**:45–62.
6. Al Tameemi W, Dale TP, Al-Jumaily RMK, Forsyth NR. Hypoxia-modified cancer cell metabolism. *Front Cell Dev Biol* 2019;**7**:4.
7. Rankin EB, Giaccia AJ. Hypoxic control of metastasis. *Science* 2016;**352**:175–80.
8. Taylor CT, Colgan SP. Regulation of immunity and inflammation by hypoxia in immunological niches. *Nat Rev Immunol* 2017;**17**:774–85.
9. Facciabene A, Peng X, Hagemann IS, Balint K, Barchetti A, Wang LP, et al. Tumour hypoxia promotes tolerance and angiogenesis *via* CCL28 and T_{reg} cells. *Nature* 2011;**475**:226–30.
10. Thienpont B, Steinbacher J, Zhao H, D'Anna F, Kuchnio A, Ploumakis A, et al. Tumour hypoxia causes DNA hypermethylation by reducing TET activity. *Nature* 2016;**537**:63–8.

11. Graham K, Unger E. Overcoming tumor hypoxia as a barrier to radiotherapy, chemotherapy and immunotherapy in cancer treatment. *Int J Nanomed* 2018;**13**:6049−58.
12. Horsman MR, Mortensen LS, Petersen JB, Busk M, Overgaard J. Imaging hypoxia to improve radiotherapy outcome. *Nat Rev Clin Oncol* 2012;**9**:674−87.
13. Hong EJ, Choi DG, Shim MS. Targeted and effective photodynamic therapy for cancer using functionalized nanomaterials. *Acta Pharm Sin B* 2016;**6**:297−307.
14. Mallidi S, Anbil S, Bulin AL, Obaid G, Ichikawa M, Hasan T. Beyond the barriers of light penetration: strategies, perspectives and possibilities for photodynamic therapy. *Theranostics* 2016;**6**:2458−87.
15. Li G, Yuan S, Deng D, Ou T, Li Y, Sun R, et al. Fluorinated polyethylenimine to enable transmucosal delivery of photosensitizer-conjugated catalase for photodynamic therapy of orthotopic bladder tumors postintravesical instillation. *Adv Funct Mater* 2019;**29**: 1901932.
16. Zhang J, Jiang C, Figueiró Longo JP, Azevedo RB, Zhang H, Muehlmann LA. An updated overview on the development of new photosensitizers for anticancer photodynamic therapy. *Acta Pharm Sin B* 2018;**8**:137−46.
17. Fu J, Wu B, Wei M, Huang Y, Zhou Y, Zhang Q, et al. Prussian blue nanosphere-embedded *in situ* hydrogel for photothermal therapy by peritumoral administration. *Acta Pharm Sin B* 2019;**9**:604−14.
18. He H, Liu L, Liang R, Zhou H, Pan H, Zhang S, et al. Tumor-targeted nanoplatform for *in situ* oxygenation-boosted immunogenic phototherapy of colorectal cancer. *Acta Biomater* 2020;**104**:188−97.
19. Liu R, An Y, Jia W, Wang Y, Wu Y, Zhen Y, et al. Macrophage-mimic shape changeable nanomedicine retained in tumor for multimodal therapy of breast cancer. *J Control Release* 2020;**321**:589−601.
20. Phua SZF, Yang G, Lim WQ, Verma A, Chen H, Thanabalu T, et al. Catalase-integrated hyaluronic acid as nanocarriers for enhanced photodynamic therapy in solid tumor. *ACS Nano* 2019;**13**:4742−51.
21. Zhang R, Song X, Liang C, Yi X, Song G, Chao Y, et al. Catalase-loaded cisplatin-prodrug-constructed liposomes to overcome tumor hypoxia for enhanced chemo-radiotherapy of cancer. *Biomaterials* 2017;**138**:13−21.
22. Song X, Xu J, Liang C, Chao Y, Jin Q, Wang C, et al. Self-supplied tumor oxygenation through separated liposomal delivery of H2O2 and catalase for enhanced radio-immunotherapy of cancer. *Nano Lett* 2018;**18**:6360−8.
23. Sun Y, Zhao D, Wang G, Wang Y, Cao L, Sun J, et al. Recent progress of hypoxia-modulated multifunctional nanomedicines to enhance photodynamic therapy: opportunities, challenges, and future development. *Acta Pharm Sin B* 2020;**10**:1382−96.
24. Sass MD. Catalase activity in young red cells. *Nature* 1963;**197**: 503−4.
25. Bukowska B, Chajdys A, Duda W, Duchnowicz P. Catalase activity in human erythrocytes: effect of phenoxyherbicides and their metabolites. *Cell Biol Int* 2000;**24**:705−11.
26. Paniker NV, Iyer GY. Erythrocyte catalase and detoxication of hydrogen peroxide. *Can J Biochem* 1965;**43**:1029−39.
27. Chen Q, Chen J, Liang C, Feng L, Dong Z, Song X, et al. Drug-induced co-assembly of albumin/catalase as smart nano-theranostics for deep intra-tumoral penetration, hypoxia relieve, and synergistic combination therapy. *J Control Release* 2017;**263**:79−89.
28. Wang H, Chao Y, Liu J, Zhu W, Wang G, Xu L, et al. Photosensitizer-crosslinked *in-situ* polymerization on catalase for tumor hypoxia modulation & enhanced photodynamic therapy. *Biomaterials* 2018; **181**:310−7.
29. Song G, Chen Y, Liang C, Yi X, Liu J, Sun X, et al. Catalase-loaded TaOx nanoshells as bio-nanoreactors combining high-Z element and enzyme delivery for enhancing radiotherapy. *Adv Mater* 2016;**28**:7143−8.
30. Cheng H, Zhu JY, Li SY, Zeng JY, Lei Q, Chen K-W, et al. An O_2 self-sufficient biomimetic nanoplatform for highly specific and efficient photodynamic therapy. *Adv Funct Mater* 2016;**26**:7847−60.
31. Chen H, Tian J, He W, Guo Z. H_2O_2-activatable and O_2-evolving nanoparticles for highly efficient and selective photodynamic therapy against hypoxic tumor cells. *J Am Chem Soc* 2015;**137**:1539−47.
32. Gilkes DM, Semenza GL, Wirtz D. Hypoxia and the extracellular matrix: drivers of tumour metastasis. *Nat Rev Canc* 2014;**14**:430−9.
33. Bertout JA, Patel SA, Simon MC. The impact of O_2 availability on human cancer. *Nat Rev Canc* 2008;**8**:967−75.
34. Zhang Z, Wang H, Tan T, Li J, Wang Z, Li Y. Rational design of nanoparticles with deep tumor penetration for effective treatment of tumor metastasis. *Adv Funct Mater* 2018;**28**:1801840.
35. Tan T, Hu H, Wang H, Li J, Wang Z, Wang J, et al. Bioinspired lipoproteins-mediated photothermia remodels tumor stroma to improve cancer cell accessibility of second nanoparticles. *Nat Commun* 2019;**10**:3322.
36. Tan T, Wang Y, Wang J, Wang Z, Wang H, Cao H, et al. Targeting peptide-decorated biomimetic lipoproteins improve deep penetration and cancer cells accessibility in solid tumor. *Acta Pharm Sin B* 2020; **10**:529−45.
37. Li C, Wang J, Wang Y, Gao H, Wei G, Huang Y, et al. Recent progress in drug delivery. *Acta Pharm Sin B* 2019;**9**:1145−62.
38. Tannock IF, Primeau A, Grantab R, Lee C. Limited penetration of anticancer drugs to cells in solid tumors: a neglected and modifiable cause of drug resistance. *J Clin Oncol* 2005;**23**:852s−s.
39. Torok S, Rezeli M, Kelemen O, Vegvari A, Watanabe K, Sugihara Y, et al. Limited tumor tissue drug penetration contributes to primary resistance against angiogenesis inhibitors. *Theranostics* 2017;**7**: 400−12.
40. Song X, Feng L, Liang C, Yang K, Liu Z. Ultrasound triggered tumor oxygenation with oxygen-shuttle nanoperfluorocarbon to overcome hypoxia-associated resistance in cancer therapies. *Nano Lett* 2016;**16**: 6145−53.
41. Jiang W, Zhang Z, Wang Q, Dou J, Zhao Y, Ma Y, et al. Tumor reoxygenation and blood perfusion enhanced photodynamic therapy using ultrathin graphdiyne oxide nanosheets. *Nano Lett* 2019;**19**: 4060−7.
42. Wang B, Zhang H, An J, Zhang Y, Sun L, Jin Y, et al. Sequential intercellular delivery nanosystem for enhancing ROS-Induced antitumor therapy. *Nano Lett* 2019;**19**:3505−18.
43. Kumar V, Gabrilovich DI. Hypoxia-inducible factors in regulation of immune responses in tumour microenvironment. *Immunology* 2014; **143**:512−9.
44. LaGory EL, Giaccia AJ. The ever-expanding role of HIF in tumour and stromal biology. *Nat Cell Biol* 2016;**18**:356.
45. Cao H, Zhang Z, Zhao S, He X, Yu H, Yin Q, et al. Hydrophobic interaction mediating self-assembled nanoparticles of succinobucol suppress lung metastasis of breast cancer by inhibition of VCAM-1 expression. *J Control Release* 2015;**205**:162−71.
46. Chen Q, Zhang XHF, Massague J. Macrophage binding to receptor VCAM-1 transmits survival signals in breast cancer cells that invade the lungs. *Canc Cell* 2011;**20**:538−49.